REFLECTING PROPERTIES OF THE SEASONALLY THAWED LAYER DURING THAWING AND FREEZING OF THE LIGHT LOAM SOIL. NUMERIC-ANALYTICAL STUDY

K. V. Muzalevsky* UDC 537.87

We use numeric-analytical methods to study theoretically the reflective properties of the layered media of the seasonally thawed active layer (AL) in the process of their freezing and thawing in the ultrawide frequency band from 10 MHz to 10 GHz, as well as the process of interaction of 2.5-ns ultrawide band pulses in the megahertz frequency range with such media, for the light loam soil with the clay-fraction weight content equal to 20% as an example. The spectral amplitudes of the reflection coefficient, the time waveforms and delays, and the propagation velocity of the pulse are calculated in the case of a monostatic radar configuration with probing the AL to the nadir by an electromagnetic wave with a plane front. It is shown that the AL soil is a low-pass filter for the reflected waves, and the cutoff frequency of this filter decreases nonlinearly with increasing AL thickness. In this case, the average frequency in the spectrum of the probing pulse decreases from 527 MHz (before the pulse enters the medium) by 38% and 23% per meter during propagation through the thawed and frozen active layers, respectively. The velocity of the ultrawideband pulse and the group velocity of the pulse propagation, which is calculated at the average frequency of the probing-pulse spectrum before the pulse enters the medium, coincide in both the thawed and frozen ALs of the light loam soil. It is shown that the energy potential of the radar system should exceed 40 dB per 0.5 m of the AL thickness in the frequency range below 1 GHz to ensure probing of the lower boundary of the AL in the freezing or thawing light loam soil. The performed studies demonstrate the basic possibility and good prospects for developing pulsed ultrawideband radar systems in the megahertz frequency range for remote probing of the geophysical parameters of the layered structure of ALs in light loam soils.

1. INTRODUCTION

The characteristics of the frozen thawed states and the freezing/thawing depth of the seasonally thawed active layer (AL) in soils are important quantities, whose monitoring is a necessary element in precision agriculture systems and which are input parameters in modern climate models. In the recent 40 years, many studies have demonstrated successfully the capabilities of microwave radar and radiometric aerospace methods used for remote probing of the above-mentioned geophysical parameters of the AL [1–4]. In the nearest future (2023), the polarimetric synthetic-aperture radar BIOMAS will be launched, and for the first time, a global orbital satellite constellation will be formed in the orbit, which will serve as the technological basis for the development of new multifrequency algorithms (similar to those in [5]) for remote probing of underlying terrains with very high frequency (VHF) waves in the ultrawide frequency band, namely, 435 MHz (BIOMAS, European Space Agency (EAS)), 1.26 GHz (ALOS-2 and ALOS-3, Japan Aerospace Exploration

* rsdkm@ksc.krasn.ru

Agency (JAXA)), 3.2 GHz (NovaSAR-1, UK), 5.4 GHz (Sentinel-1, ESA), and 9.6 GHz (TerraSAR-X, ESA and MeteoSAR, Roscosmos (Russia)) [6]. Additionally, recent intense research has been aimed at studying the possibilities of passive radar using the signals of mobile communication satellites in an VHF band, namely, 137 MHz (ORBCOMM), 240–270 MHz and 360–380 MHz (Mobile Use Objective System (MUOS)), 2.3 GHz (XM Satellite Radio), and signals at frequencies of 1.2 and 1.6 GHz (GLONASS and GPS) for the purposes of probing the soil humidity, water equivalent of the snow cover [7–11], and the thawed and frozen soil states [12, 13]. (Note that the signals from the "Gonets-D1M" communication satellites at a frequency of 390 MHz [14] can also be used for remote probing of underlying terrains.) New methods are studied for the purposes of ultrawideband radiometry, pulsed (autocorrelation) radiometry, and radar in the VHF band for remote probing of the temperature profiles of Greenland's glaciers (12 frequencies in the range from 0.5 GHz to 2 GHz are used) and the ice thickness on fresh-water lakes [15, 16], as well as for assessment of the vertical distribution of humidity in the soil of agricultural fields to a depth of up to 2.5 m [17] using the IMARK multifrequency (140 MHz, 430 MHz, 1.3 GHz, and 8.6 GHz) polarimetric synthetic-aperture radar manufactured by Vega Radio Engineering Corporation [18].

However, low resolution of modern satellite radiometers (about 40 km) and low periodicity of satellite radar surveys (approximately 12–40 days), as well as the high cost of operations of the aircraft carriers do not allow one currently to perform online monitoring and measure spatial variations of the thawed/frozen states, freezing/thawing depths, humidity of the soil ALs within individual agricultural fields, and separate landscape and soil variations. The existing limitations for application of satellite carriers can be overcome by using ultralight air drones having a gross weight below 5 kg and an outreach of up to several kilometers and equipped with microwave radiometric or radar [19–23] systems with high spatial resolution. Analysis of the publications outside Russia has shown that application of ultrawideband pulsed signals along with the methods of georadar subsurface probing and antenna aperture synthesis [23–25] is a promising new field of using radars carried by small air drones for probing the humidity [26, 27] and conductivity [28] of soils and deformations of soil surfaces (by the radar interferometry methods) [29], monitoring of glacier taliks [30] and the thickness and density of the snow cover [31, 32], detection of mine fields [25, 33–35], and determination of the top soil thickness [36]. The performed analysis of the papers published in the recent decades demonstrate the general trend for both spectrum widening and the shift of minimum operating frequencies of the aerospace systems for radar and radiometric remote probing of the Earth to the megahertz frequency region.

At the same time, the processes of interaction of VHF waves and ultrawideband megahertz pulses with layered frequency-dispersive soil ALs are insufficiently studied. This fact will not make it possible to improve the accuracy of measuring the thawed/frozen states and the depth of freezing/thawing of soil ALs on the basis of the existing methods of satellite radar and radiometry, or subsurface georadar (in the case of simple installation of modern subsurface georadars on one or two air drones in the mono- or bistatic radio ranging configuration).

Indeed, up to now the frequency dispersion of the complex dielectric permittivity of the soil ALs has not been taken into account when interpreting the data of satellite radar and subsurface georadar probing in the VHF band [4, 37]. Meanwhile, the soils with high contents of organic or clay fractions have significant variations in the complex dielectric permittivity depending on the frequency of the electromagnetic field (especially in the megahertz frequency range), which are determined mainly by the Maxwell–Wagner relaxation of the molecules of adsorbed water [38, 39], as well the ohmic conductivity of free and adsorbed water [40]. In such soils having a frequency dispersion of the complex dielectric permittivity, one observes distortions in the spectrum and time waveform of the probing pulse, as it propagates through the soil, due to stronger damping of high-frequency harmonics. As a result, the average frequency of the spectrum of the probing pulse shifts to the low-frequency region. It was demonstrated for model media [41; Table 3] that the average frequency of the probing pulse decreases from approximately 646–645 MHz to 586–587 MHz as the contents of bentonite clay increases from 0% to 25%. Hence, the probing pulse, which has passed different distances in the same medium, has different velocities and spectra, which can lead to errors in assessing dielectric properties and the AL thickness. Additionally, when using the expression for the phase

velocity [42, 43] of monochromatic waves (rather than the group velocity at the average frequency of the probing pulse, which has passed along the entire path) an unmanageable error is introduced to the estimate of the dielectric properties of soil ALs at the center operating frequency of the radar antennas due to the frequency dispersion of the complex dielectric permittivity of wet soils [44; pp. 17–18].

In this work, we study theoretically the interaction of VHF waves and ultrawideband megahertz pulses with the layered AL media in the process of freezing/thawing for light loam soils with a clay-fraction weight content equal to 20% using numeric-analytical methods. In the VHF band, the spectral reflective properties and amplitude-frequency characteristics of soil ALs are studied and the degree of distortion of time waveforms, variations in the spectral content, time delays, and velocities of propagation of ultrawideband pulses in thawed and frozen AL soils are estimated.

2. MODEL OF REFLECTION OF A PLANE ELECTROMAGNETIC WAVE FROM THE THAWED (FROZEN) SOIL ACTIVE LAYER
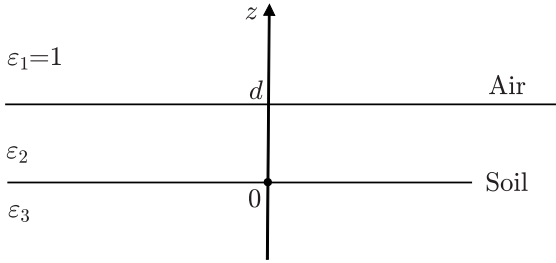

Fig. 1. Geometry of the problem.

Let the thawed or frozen soil layer with thickness d lie on the plane interface $z = 0$ m between air and a homogeneous dielectric half-space of the completely frozen or thawed soil covering. The geometry of the problem is shown in Fig. 1. The complex dielectric permittivity of the layered half-space is represented as

$$\varepsilon(z, f) = \begin{cases} 1, & d < z; \\ \varepsilon_1(T_s, W, C, \rho_d, f), & 0 \leq z \leq d; \\ \varepsilon_2(T_s, W, C, \rho_d, f), & z \leq 0. \end{cases} \quad (1)$$

Here, T_s is the temperature, W is the volume humidity, C is the clay-fraction content, ρ_d is the density of the dry soil consistency, and f is the wave frequency. In what follows, we will assume that a plane electromagnetic wave is incident on the layer vertically from the upper half-space ($z > d$). Then, the spectrum of the coefficient $R(f)$ of the wave reflection from the layered inhomogeneous half-space described by Eq. (1) can be calculated in the boundary plane $z = d + 0$ m by the Brekhovskikh iterative method [45]. Roughness of the soil surface and the vegetative cover were not taken into account in these calculations. When calculating the reflection coefficient $R(f)$, we used the refraction model of complex dielectric permittivity of the soil [46]:

$$\frac{n_s(T_s, W, C, \rho_d, f) - 1}{\rho_d} = \begin{cases} \dfrac{n_m - 1}{\rho_m} + \dfrac{n_b(T_s, f) - 1}{\rho_b} m_g, & m_g \leq m_{g1}(T_s, C); \\ \dfrac{n_m - 1}{\rho_m} + \dfrac{n_b(T_s, f) - 1}{\rho_b} m_{g1}(T_s, C) + \dfrac{n_{u,i}(T_s, f) - 1}{\rho_{u,i}} [m_g - m_{g1}(T_s, C)], \\ \qquad\qquad m_g > m_{g1}(T_s, C), \end{cases} \quad (2a)$$

$$\frac{\kappa_s(T_s, W, C, \rho_d, f)}{\rho_d} = \begin{cases} \dfrac{\kappa_m}{\rho_m} + \dfrac{\kappa_b(T_s, f)}{\rho_b} m_g, & m_g \leq m_{g1}(T_s, C); \\ \dfrac{\kappa_m}{\rho_m} + \dfrac{\kappa_b(T_s, f)}{\rho_b} m_{g1}(T_s, C) + \dfrac{\kappa_{u,i}(T_s, f)}{\rho_{u,i}} [m_g - m_{g1}(T_s, C)], \\ \qquad\qquad m_g > m_{g1}(T_s, C), \end{cases} \quad (2b)$$

where the refractive index n and the normalized attenuation coefficient κ are related to the real and imaginary parts (ε' and ε'', respectively) of the complex dielectric permittivity ε by the expressions

$$n = \frac{1}{\sqrt{2}}\sqrt{\sqrt{\varepsilon'^2 + \varepsilon''^2} + \varepsilon'}, \qquad \kappa = \frac{1}{\sqrt{2}}\sqrt{\sqrt{\varepsilon'^2 + \varepsilon''^2} - \varepsilon'}.$$

The subscripts s, m, b, u, and i refer to the soil, mineral particles, bound water, free water, and ice on the soil, respectively. The total water content and the maximum content of bound water in the soil by weight are denoted as m_g and m_{g1}, respectively. Particular values of the parameters and the MATLAB code for the calculation of the complex dielectric permittivity of the soil in accordance with the model of Eqs. (2a) and (2b) can be found in [46, 47]. The model in [46] makes it possible to calculate the complex dielectric permittivity of the soil covering as a function of the density ρ_d of the dry soil consistency, the weight humidity $M_g = W/\rho_d$ (from 0.02 to 0.33), the clay-function content C (approximately from 9% to 42% by weight), and the soil temperature T_s (from $-30°$ C to $+25°$). In further calculations, the temperature of the frozen and thawed soil was put equal to $T_s^{fr} = -8\,°C$ and $T_s^{th} = 20\,°C$, respectively. The dielectric model [46] is based on soil samples taken from the mineral horizon of tundra soils, in which the content of the clay fraction varied from 9.1% to 41.3% (by weight), and the content of the organic matter was insignificant and varied from 0.9 to 4.1% (by weight). Due to the fact that the content of the clay fraction determines the temperature and frequency dependences of the complex dielectric permittivity of nonsaline soils in the radio-frequency range above 10–40 MHz [46, 48], in this paper we perform an analysis for the model of light loam agricultural mineral soil with a soil-fraction content equal to 20% using the model in [46]. The density of the dry soil consistency was specified by the average value $\rho_d = 1.03$ g/cm^3 of the experimentally measured densities of the dry AL soil consistency in the layer (0–30 cm) on an agricultural field near the village of Minino in Krasnoyarsk Region [49].

The time waveform $s(t)$ of an electromagnetic pulse with a plane wave front (the quantity proportional to the horizontal component E_y of the electric field), which is reflected from the AL, can be calculated using the convolution integral and the Fourier transform:

$$s(t) = \int\limits_0^{t_{max}} s_0(\tau)g(t-\tau)\,d\tau, \qquad g(t) = 2\mathrm{Re}\int\limits_0^\infty R(f)\exp(-2\pi i f t)\,df. \qquad (3)$$

Here, t is the current time, t_{max} is the maximum readout on the time scale (much longer than the pulse duration), and $g(t)$ is the impulse response of the probed medium. The pulse $s_0(t)$ at the input to the medium was specified with accuracy up to a constant in the form of the second derivative of the Gaussian function:

$$s_0(t) = -\left[2\left(\frac{t-t_0}{\Delta t}\right)^2 - 1\right]\exp\left(-\frac{t-t_0}{\Delta t}\right)^2, \qquad (4)$$

where t_0 is the shift of the pulse center along the time scale relative to the scale origin, and Δt is the half-width of the Gaussian function at the level -8.7 dB. Integrals (3) were evaluated numerically. The integration interval was divided into 100 segments both in the frequency and time regions, and the Gaussian quadrature with 24 nodes was applied in each of the segments [50]. Such partition ensured an absolute error of no worse than 10^{-6} for evaluation of integrals (3). In the subsequent calculations, the value of Δt was put equal to 0.6 ns, which allowed one to form a probing pulse with a duration of 2.5 ns (at the 0.1 level), whose spectrum covers the frequencies from 256 MHz to 868 MHz (at the -6 dB level) with an average frequency of 527 MHz. The characteristics of the formed pulse are close to those of the pulses emitted by commercial georadar antennas used onboard air drones [51, 52]. The spectrum width and the waveform of the probing pulse are presented in Fig. 2.

3. REFLECTIVE PROPERTIES OF THE FROZEN (THAWED) SOIL ACTIVE LAYER

Using the dielectric soil model [46], we calculate the frequency spectra of the magnitude of the reflection coefficient for an AL of different thicknesses (see Fig. 3) in the cases of its freezing (a frozen layer over a thawed half-space) and thawing (a thawed layer over a frozen half-space). One can easily see the interference pattern in the frequency dependence of the magnitude of the reflection coefficient (the dotted and dashed
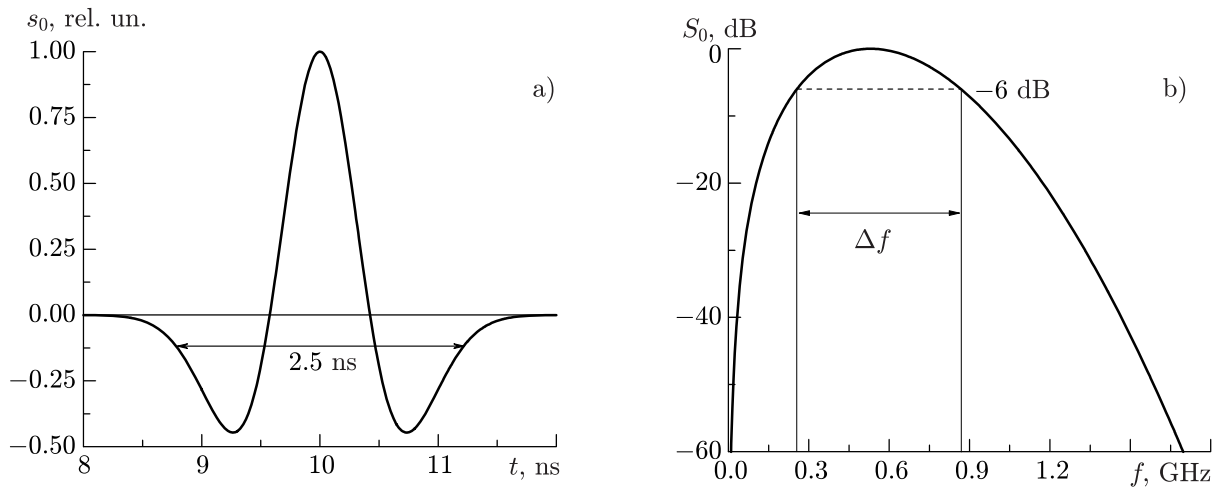
Fig. 2. Time waveform $s_0(t)$ (*a*) and the spectrum $S_0(f)$ (*b*) of the probing ultrawideband pulse with a duration of 2.5 ns and $\Delta f = 0.612$ GHz.
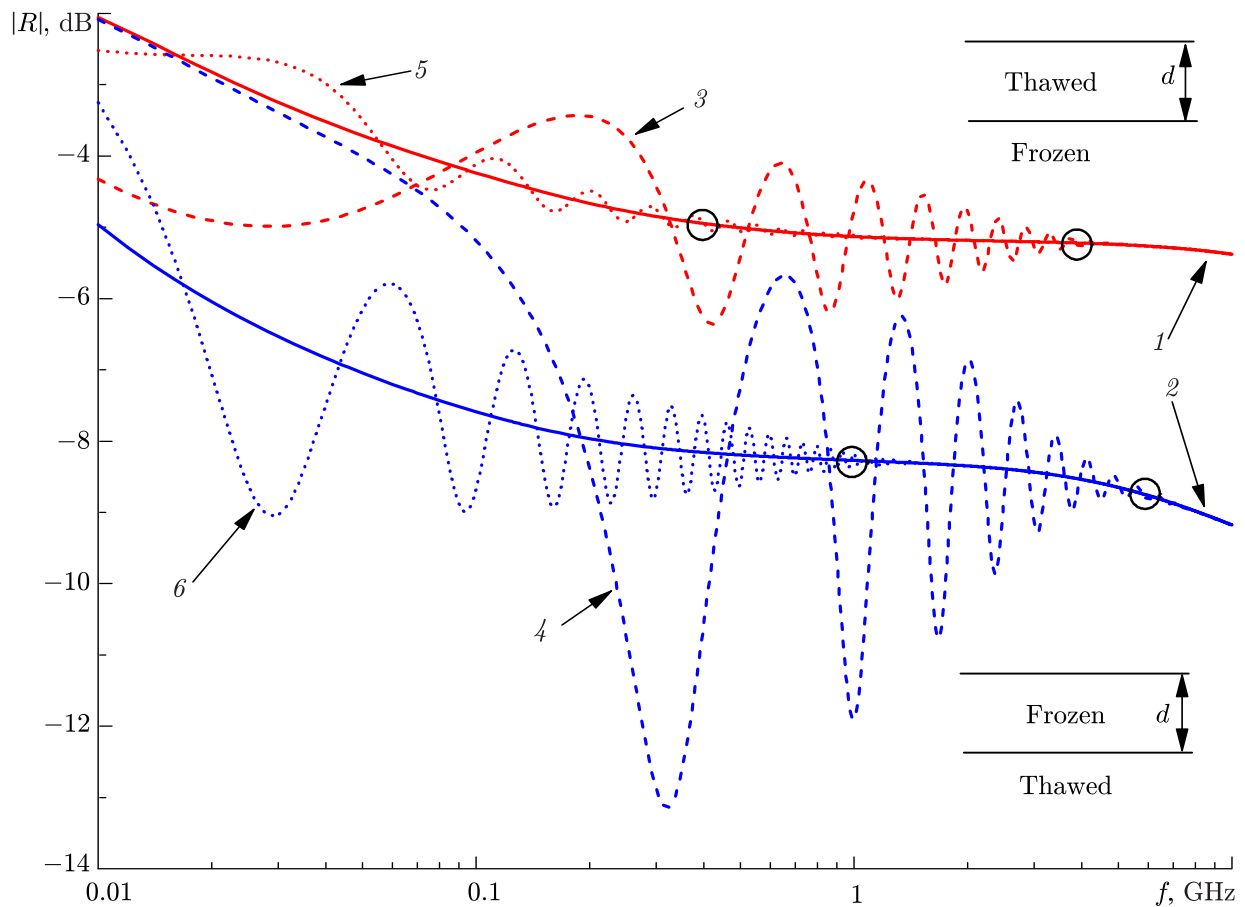

Fig. 3. Spectrum of the reflection-coefficient magnitude $|R|$ for the completely thawed and the completely frozen ALs (the solid red line *1* and the solid blue line *2*, respectively). The dashed and dotted lines show the spectra for different thicknesses of the thawing and freezing ALs (red and blue colors, respectively): $d = 0.1$ m (lines *3* and *4*), $d = 0.5$ m (line *5*), and $d = 1$ m (line *6*). The figure also shows schematically the configurations of the layered medium, which correspond to the red and blue lines.

lines *3–6* in Fig. 3) relative to its values in the cases of reflection from a completely thawed or completely frozen soil (the red solid line *1* and the blue solid line *2*, respectively in Fig. 3). For the thawed layer,

a lower amplitude of the interference oscillations is observed as compared with the frozen layer due to stronger damping of the wave in the thawed soil. As the frequency rises, the amplitude of interference oscillations tends to zero due to the stronger wave damping at the increasing optical thickness of the probed layer. The coefficient of wave reflection from a frozen layer having a thickness $d < 0.1$ m coincides with the coefficient of wave reflection from the completely thawed soil at frequencies below 10–30 MHz (the dotted blue line 4 and the red solid line 1 in Fig. 3). It is also seen in Fig. 3 (see the black circles) that depending on the AL thickness, there exists a maximum frequency that limits the interference pattern with respect to the amplitude level in the high-frequency region (for definiteness, this level is specified at ± 0.1 dB). We will call this frequency f_m the maximum frequency of the interference occurrence. Above this frequency, the interference phenomenon can be neglected, and the medium can be regarded as a homogeneous half-space with the dielectric permittivity of the AL. As the layer thickness increases, the frequency f_m shifts to the low-frequency region (see Fig. 3 and the red and blue dashed lines in Fig. 4 for the
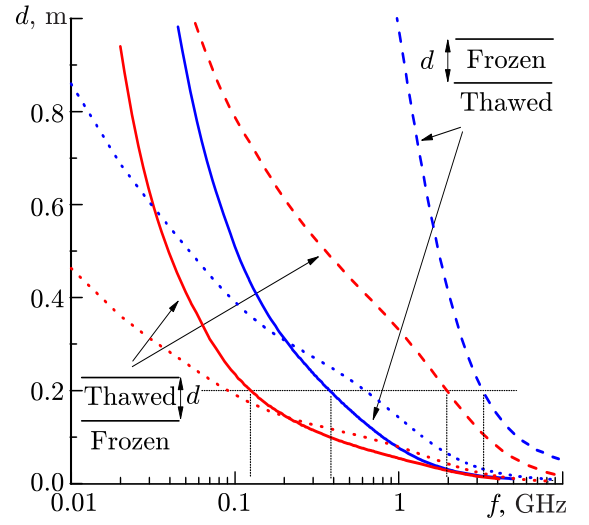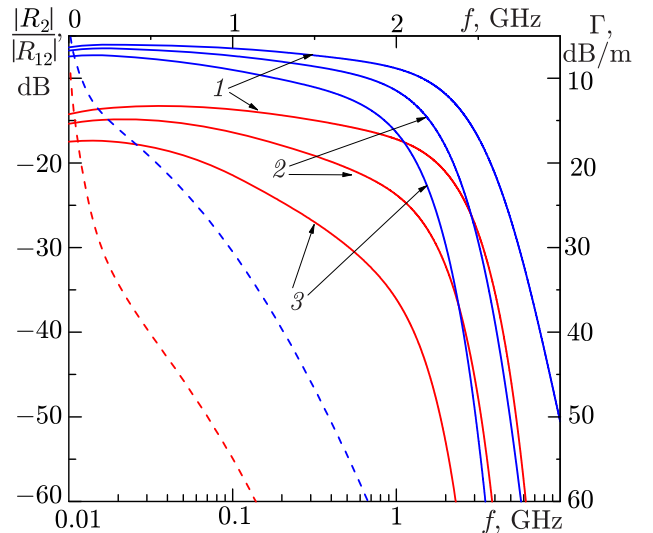

Fig. 4. The cutoff frequency of the low-pass filter (solid lines) and the maximum frequency of the interference occurrence (dashed lines) in the cases of thawing (red color) and freezing (blue color) of the AL. The corresponding dotted lines show the calculated skin depth $1/(2k_0\kappa_2)$.

thawed or frozen layer, respectively), i.e., high frequencies are filtered out as the wave propagates through the layer.

In order to assess the character of the amplitude-frequency characteristic of the probed medium, we calculate the magnitude of the coefficient $R_2(f)$ of wave reflection from the lower boundary of the layer (with account for the double passage of the wave through the AL) and present it normalized to the magnitude of the coefficient $R_{12}(f)$ of wave reflection from the interface of air and the upper layer boundary:

$$R_2(f) = [1 - R_{12}^2(f)]R_{23}(f)\exp(2ik_0\sqrt{\varepsilon_2}d), \qquad (5)$$

where k_0 is the wave number in free space, d is the layer thickness, and $R_{23}(f)$ is the coefficient of wave reflection from the lower layer boundary (see the solid lines in Fig. 5). It is is seen in Fig. 5 that as the thickness d of the layer increases, the frequency dependence of $|R_2|/|R_{12}|$ has the character of a low-pass

Fig. 5. Magnitude of the coefficient of wave reflection from the lower boundary of the AL with allowance for the double passage of the layer and normalization to the magnitude of the coefficient of wave reflection from the upper boundary of the AL (solid lines) at $d = 0.07$ (lines 1), 0.15 m (2), and 0.3 m (3). The dashed line shows the coefficient of specific wave damping during propagation in AL soils, which is calculated by the formula $\Gamma(f) = 20(\log e) k_0\kappa_2$ (presented on a semi-logarithmic scale, with the corresponding frequency axis on the top of the plot). The red and blue colors correspond to the thawed and frozen soils, respectively.

filter in the cases of both thawed and frozen ALs. The cutoff frequencies of this filter at a level of -3 dB decrease nonlinearly with increasing AL thickness (the red and blue solid lines for the thawed and frozen soil layer, respectively, in see Fig. 4). Note that for practical applications, the AL probing thickness can be calculated approximately on the basis of evaluating the skin depth $l_{\mathrm{eff}} = 1/(2k_0\kappa_2)$ and allowing for the double passage of the wave through the layer bulk. The difference between the estimates of the probing-layer thickness on the basis of the cutoff frequency of the low-pass filter and the skin depth (see the solid and dashed lines in Fig. 4) are determined by variations in the amplitudes of the waves reflected from the upper and lower boundaries due to the frequency dependence of the reflection coefficients.

As a result, two criteria can be proposed for choosing the maximum frequency in the spectrum of the probing pulse, namely, a stricter criterion based on the analysis of the medium as an equivalent of the low-pass filter (with wave damping at a level of -3 dB) and a softer criterion based on the analysis of the maximum frequency of the interference occurrence (see Fig. 4).

Note that even in the case of a frozen soil, the phenomena of frequency dispersion is observed for the magnitude of the coefficient of reflection from the AL (the solid line *2* in Fig. 3), which affects the probing depth significantly (see Fig. 4). Thus, during propagation through a frozen and thawed soil, the wave damping increases nonlinearly by more than 40 dB/m per decade as the frequency rises (see the dashed lines on a semilogarithmic scale in Fig. 5). The nonlinear damping of the waves with increasing frequency (in the frequency range of the probing-pulse spectrum; see the dashed lines in Fig. 5) is determined by the phenomenon of frequency dispersion of the dielectric permittivity of bound water, whose quantity in a nonsaline soil depends on the soil type (contents of the clay fraction and organic matter) and temperature [46, 48].
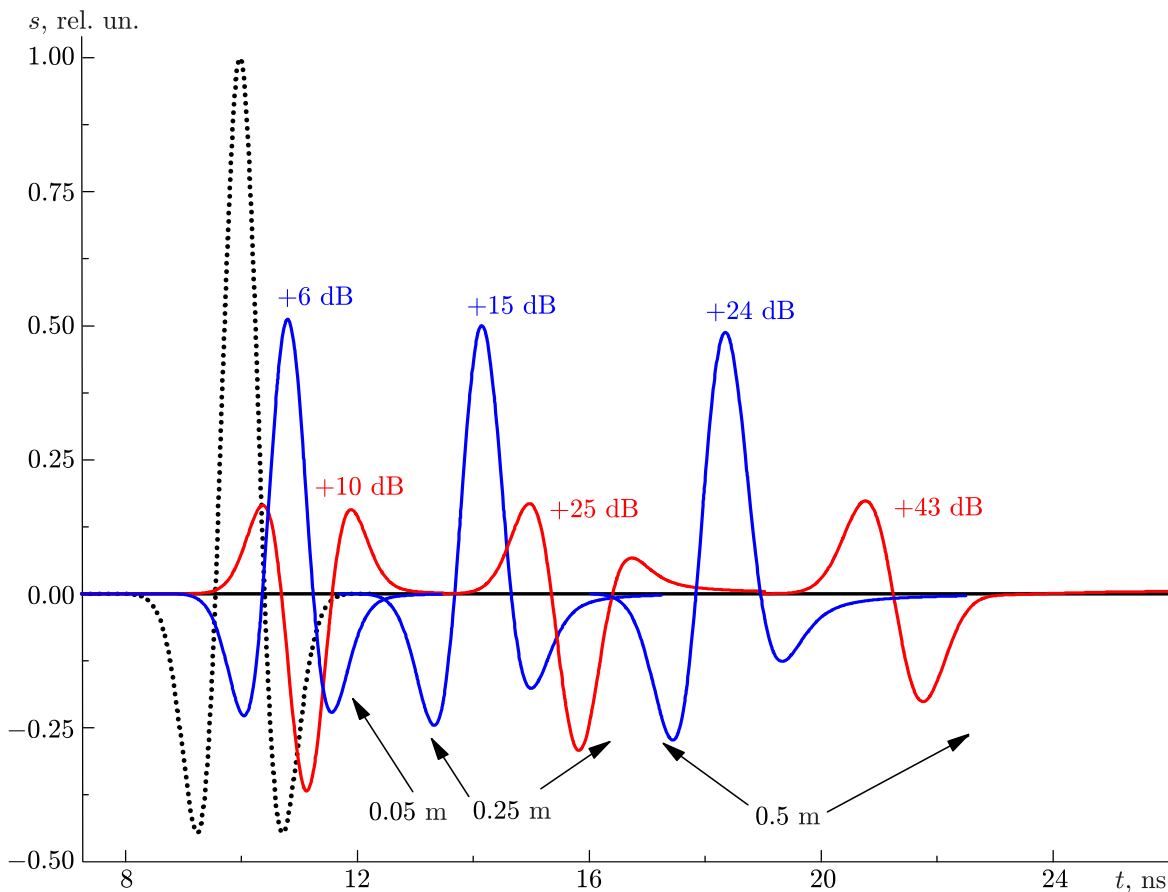

Fig. 6. Time waveforms of the initial pulse (dotted line) and probing pulses reflected from the thawed (red color) and frozen (blue color) AL with different thicknesses. The pulse amplitudes are amplified for each AL thickness (see the legend of the lines).

704

4. PROPAGATION VELOCITY AND DISTORTION OF PULSES DURING PROPAGATION THROUGH A THAWED (FROZEN) ACTIVE LAYER

We now consider the time waveforms of a tripolar probing pulse (see Fig. 2a) reflected from the thawed (frozen) soil AL having different thicknesses (see Fig. 6). In order to perform a more detailed analysis of the time waveforms of the pulses reflected from the lower boundary of the layer and passing through the layer two times, we will calculate these waveforms by formulas (3) using Eq. (5) for the reflection coefficient.

For the pulse propagating through a thawed soil, the damping is stronger by approximately 10 dB per each 0.25 m of the layer thickness and the propagation time is 1.7 ns longer compared with the pulse propagating through the frozen soil layer (see Fig. 6). The tripolar shape of the initial pulse is preserved in the case of probing the frozen layer with a thickness greater than 0.5 m and it is destroyed in the case of probing the thawed layer with a thickness greater than 0.25 m. During propagation
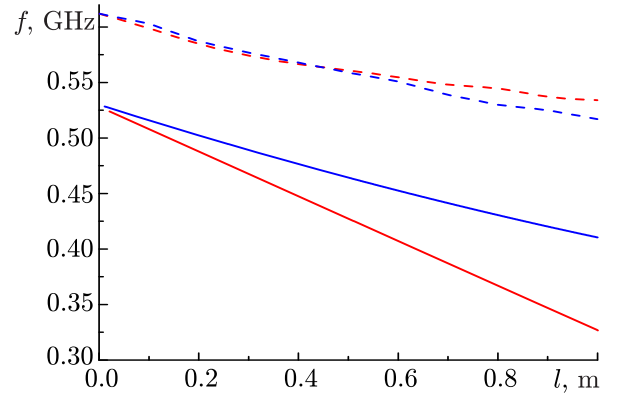

Fig. 7. Average frequency (solid lines) in the probing-pulse spectrum and the width of this spectrum (dashed lines) as functions of the distance $l = 2d$ passed by the pulsed in the thawed (red) and frozen (blue) ALs.

through the thawed and frozen layer, the average frequency of the probing pulse (see the solid lines in Fig. 7) decreases by 203 MHz/m and 120 MHz/m, i.e., 38% and 23% of the average frequency of the probing pulse (before it enters the medium), respectively. The width of the spectrum of the probing pulse propagating in both the thawed and frozen layers decreases by about 87 MHz/m (the dashed lines in see Fig. 7), i.e., 14% of the initial spectrum width (612 MHz) of the probing pulse.

For the considered light loam soils, the group velocity of pulse propagation in the thawed and frozen soils is almost independent of the frequency in the range from about 200 MHz to 1 GHz (see the dashed lines in Fig. 8a), which determines weak distortions of the time waveforms of probing pulses during their propagation in the soil ALs. For accurate calculations and interpretation of georadar probing data in such soils, one should assume that the velocity of the pulse propagation is equal to the group velocity (see the solid and dashed lines in Fig. 8b) calculated at the average frequency of the pulse (before it enters the medium). In the case of a frozen layer, it is possible to use the phase velocity calculated at the average frequency of
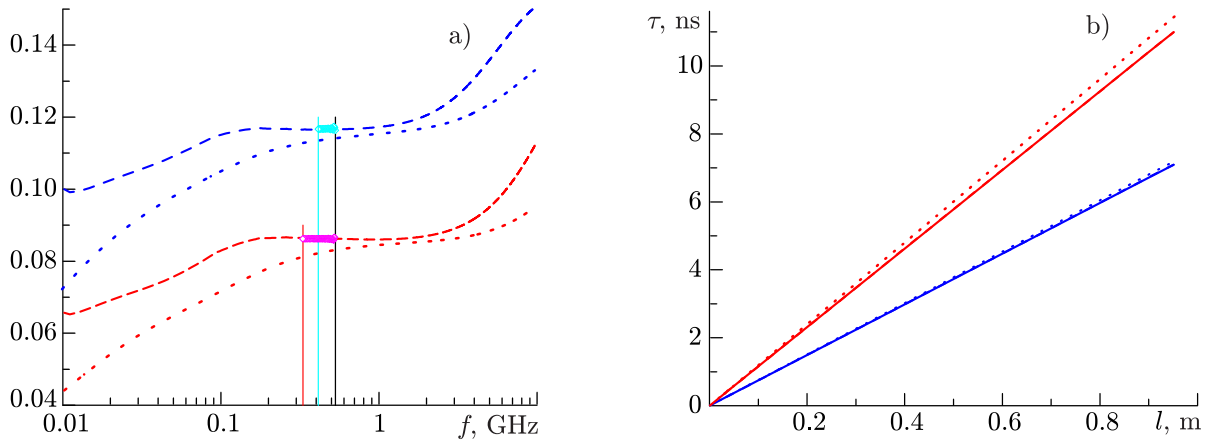

Fig. 8. (a) The normalized (to the speed of light in free space) group velocity (dashed lines), the phase velocity (dotted lines), and the pulse velocity (blue and crimson symbols), which is calculated as the ratio of the distance $l = 2d$ to the propagation time of the pulse-envelope maximum) (a) and the propagation time τ of the reflected pulse with these velocities through the thawed and frozen ALs (red and blue color, respectively) (b).

the pulses (before they enter the medium) to estimate the pulse propagation velocity, since this velocity is close to the phase velocity of the wave at the average frequency of the pulse (see the solid and dashed blue lines in Fig. 8b). In the case of a thawed soil, the pulse propagation velocity differs from the phase velocity by about 4.7%/m, which can lead to underrated estimates of the AL thickness by about 5 cm per each 0.5 m of the layer thickness.

5. CONCLUSIONS

The frequency dispersion of the complex dielectric permittivity of the AL in a light loam soil distorts the frequency spectrum and the time waveform of the probing pulse and reduces the average frequency and width of the spectrum of the pulse, as it propagates through both the thawed and frozen ALs. The decrease in the average frequency of the probing pulse reflected from the AL, which was found in the simulation process, is indicative of the necessity to make frequency-detuned receiving and transmitting antennas. Note that even when the pulse is reflected from the frozen AL, its average frequency (527 MHz) decreases by 23%/m and the width of the pulse spectrum (612 MHz) decreases by 14%/m compared with the corresponding characteristics of the initial probing pulse. Due to this fact, the average operating frequency of the receiving antenna should be chosen to be several hundreds of megahertz lower than that of the transmitting antenna, which allows one to expand the total dynamic range of georadars and reduce distortions in the recorded temporal shapes of the pulses reflected from the AL. The simulation also shows that for precision calculations of the thickness of the AL in thawed and frozen light loam soils, the pulse propagation velocity should be evaluated on the basis of the group velocity, rather than the phase velocity. (In these estimates, one can use the average frequency of the probing-pulse spectrum at the entrance to the medium.)

The interference pattern, which is observed in the frequency dependence of the magnitude of the coefficient of reflection from the thawed and frozen AL soils, is limited by a certain maximum frequency decreasing with increasing AL thickness. Additionally, it has been found that the AL soils for the reflected VHF waves are equivalent to a low-pass filter whose cutoff frequency decreases nonlinearly with increasing AL thickness. As a result, the frequency of the interference occurrence (when passing from higher frequencies to lower ones) and the cutoff frequency of such a filter can be recommended as criteria for the choice of the maximum and minimum frequencies in the spectrum of the waves probing light loam AL soils. Further substantiation of this proposal requires additional studies of the wave spectrum and shapes of the probing pulses for a wider group of soils (with different densities, humidities, and granulometric compositions).

A significant difference in the magnitudes of the coefficient of wave reflection from the completely frozen and completely thawed soils (about 4 dB), as well as the considerable difference in the magnitudes of the coefficient of wave reflection from the upper and lower AL boundaries (at least -40 dB per 0.5 m of the AL thickness at $f < 1$ GHz) indicate that it is essentially possible to develop multifrequency radar and ultrawideband pulsed systems operating in the megahertz frequency range for remote probing of geophysical parameters of the layered structures in the upper parts of ALs in light loam soils.

REFERENCES

1. Y. Yi, J. S. Kimball, R. H. Chen, et al., *Cryosphere*, **12**, 145–161 (2018). https://doi.org/10.5194/tc-12-145-2018

2. X. Zhang, H. Zhang, C. Wang, et al., *IEEE Access*, **8**, 84336–84351 (2020). https://doi.org/10.1109/ACCESS.2020.2988482

3. B. Widhalm, A. Bartsch, M. Leibman, and A. Khomutov, *Cryosphere*, **11**, 483–496 (2017). https://doi.org/10.5194/tc-11-483-2017

4. A. D. Parsekian, R. H. Chen, R. J. Michaelides, et al., *Remote Sens.*, **13**, 2876 (2021). https://doi.org/10.3390/rs13152876

5. N. G. Zerdev and G. P. Kulemin, *Issled. Zemli Kosmosa*, **1**, 90–95 (1993).

6. https://space.oscar.wmo.int/instruments

7. J. L. Garrison, R. Shah, B. Nold, et al., in: *2021 IEEE Int. Geoscience and Remote Sensing Symp. (IGARSS), July 11–16, 2021, Brussels, Belgium*, pp. 164–167. https://doi.org/10.1109/IGARSS47720.2021.9554546

8. D. R. Boyd, A. C. Gurbuz, M. Kurum, et al., *IEEE J. Sel. Top. Appl. Earth Obs. Remote Sens.*, **13**, 6101–6114 (2020). https://doi.org/10.1109/JSTARS.2020.3029158

9. A. Lwin, D. Yang, X. Hong, et al., *Climate*, **9**, 175 (2021). https://doi.org/10.3390/cli9120175

10. H. Carreno-Luengo, S. Lowe, C. Zuffada, et al., *Remote Sens.*, **9**, 362 (2017). https://doi.org/10.3390/rs9040362

11. S. Yueh, R. Shah, X. Xu, et al., *Proc. SPIE*, **10785**, 107850B (2018). https://doi.org/10.1117/12.2325819

12. X. Wu, Z. Dong, S. Jin, et al., *Remote Sens.*, **12**, 2361 (2020). https://doi.org/10.3390/rs12152361

13. D. Comite, L. Cenci, A. Colliander, and Pierdicca, *IEEE J. Sel. Top. Appl. Earth Obs. Remote Sens.*, **13**, 2996–3005 (2020). https://doi.org/10.1109/JSTARS.2020.2986859

14. https://gonets.ru/rus/

15. C. Yardim, J. T. Johnson, K. C. Jezek, et al., *IEEE Trans. Geosci. Remote Sens.*, **60**, Art. no. 4300312 (2022). https://doi.org/10.1109/TGRS.2020.3043954

16. M. Salim, R. De Roo, M. J. Andrews, et al., in: *IEEE Int. Geoscience and Remote Sensing Symp. (IGARSS), July 11–16, 2021, Brussels, Belgium*, pp. 1031–1034. https://doi.org/10.1109/IGARSS47720.2021.9553970

17. B. G. Kutuza, ed., "Surface and subsurface cover probing using a multifrequency polarimetric synthetic aperture radar", Report on Research Project No. 01201280948 [in Russian], Inst. Radioengin. Electron., Moscow (2015).

18. B. Kutuza, A. Davidkin, A. Dzenkevich, et al., in: *1st Eur. Radar Conf. EuRAD, October 11-15, 2004, Amsterdam, Netherlands*, pp. 5–12.

19. A. M. Shutko, S. P. Golovachev, E. P. Novichikhin, et al., in: *2006 IEEE MicroRad February 28—March 3 2006, San Juan, USA*, pp. 82–86. https://doi.org/10.1109/MICRAD.2006.1677067

20. R. Acevo-Herrera, A. Aguasca, X. Bosch-Lluis, et al., *Remote Sens.*, **2**, 1662–1679 (2010). https://doi.org/10.3390/rs2071662

21. E. Dai, A. Venkitasubramony, A. Gasiewski, et al., in: *2018 IEEE Int. Geoscience and Remote Sensing Symp. (IGARSS 2018), July 22–27, 2018, Valencia, Spain*, pp. 6496–6499. https://doi.org/10.1109/IGARSS.2018.8518730

22. M. Troglia Gamba, G. Marucco, M. Pini, et al., *Sensors*, **15**, 28287–28313 (2015). https://doi.org/10.3390/s151128287

23. M. Schartel, K. Prakasan, P. Hügler, et al., in: *2018 IEEE Int. Geoscience and Remote Sensing Symp. (IGARSS 2018), July 22–27, 2018, Valencia, Spain*, pp. 5420–5423. https://doi.org/10.1109/IGARSS.2018.8518905

24. X. Zhang, Z. Shao, J. Ren, et al., in: *2018 IEEE Int. Geoscience and Remote Sensing Symp. (IGARSS 2018), July 22–27, 2018, Valencia, Spain*, pp. 7825–7828. https://doi.org/10.1109/IGARSS.2018.8519235

25. M. García Fernández, Y. Álvarez López, A. Arboleya Arboleya, et al., *IEEE Access*, **6**, 45100–45112 (2018). https://doi.org/10.1109/ACCESS.2018.2863572

26. https://esto.nasa.gov/forums/estf2021/Presentations/June24/Moghaddam_GPR_ESTF2021.pdf

27. K. Wu, G. Arambulo Rodriguez, M. Zajc, et al., *Remote Sens. Environ.*, **235**, 111456 (2019). https://doi.org/10.1016/j.rse.2019.111456

28. K. Wu, E. Jacquemin, L. Palt, et al., in: *NSG2021 27th Eur. Meeting of Environmental and Engineering Geophysics, August 29—September 2, 2021, Bordeaux, France*, pp. 1–5. https://doi.org/10.3997/2214-4609.202120117

29. D. Luebeck, C. Wimmer, L. F. Moreira, et al., *Remote Sens.*, **12**, No. 5, 778 (2020). https://doi.org/10.3390/rs12050778

30. G. Church, A. Bauder, M. Grab, and H. Maurer, *Cryosphere*, **15**, 3975–3988 (2021). https://doi.org/10.5194/tc-15-3975-2021

31. R. O. R. Jenssen and S. K. Jacobsen, *Remote Sens.*, **13**, 2610 (2021). https://doi.org/10.3390/rs13132610

32. K. V. Myzalevskiy, *Zh. Radioélectron.*, **8**, 1 (2021) https://doi.org/10.30898/1684-1719.2021.8.1

33. D. Šipoš and D. Gleich, *Sensors*, **20**, No. 8, 2234 (2020). https://doi.org/10.3390/s20082234

34. M. García-Fernández, G. Álvarez-Narciandi, Y. Álvarez López, and F. Las-Heras, *ISPRS J. Photogramm. Remote Sens.*, **189**, 128–142 (2022). https://doi.org/10.1016/j.isprsjprs.2022.04.014

35. A. Heinzel, M. Schartel, R. Burr, et al., *Proc. SPIE*, **11003**, 1100304 (2019). https://doi.org/10.1117/12.2518587

36. J. Hou, Y. Yan, and P. Cong, *IOP Conf. Ser. Earth Environ. Sci.*, **719**, No. 4., 042074 (2021). https://doi.org/10.1088/1755-1315/719/4/042074

37. M. Sudakova, M. Sadurtdinov, A. Skvortsov, et al., *Remote Sens.*, **13**, Art. no. 3271 (2021). https://doi.org/10.3390/rs13163271

38. V. L. Mironov, A. Yu. Karavayskiy, Yu. I. Lukin, and I. P. Molostov, *Int. J. Remote Sens.*, **41**, No. 10, 3845–3865 (2020). https://doi.org/10.1080/01431161.2019.1708506

39. P. P. Bobrov, T. A. Belyaeva, E. S. Kroshka, and O. V. Rodionova, *Euras. Soil Sci.*, **52**, No. 7, 822–833 (2019). https://doi.org/10.1134/S106422931905003X

40. P. P Bobrov, O. V. Kondratyeva, and M. M. Mustakova, *Bull. M. F. Reshetnev Sibirsk. State Aerospace Univ.*, **5**, No. 51, 95–97 (2014).

41. F. Tosti, C. Patriarca, E. Slob, et al., *J. Appl. Geophys.*, **97**, 69–80 (2013). https://doi.org/10.1016/j.jappgeo.2013.04.006

42. L. K. Clayton, K. Schaefer, M. J. Battaglia, et al., *Environ. Res. Lett.*, **16**, 055028 (2021). https://doi.org/10.1088/1748-9326/abfa4c

43. M. S. Sudakova, M. R. Sadurtdinov, G. V. Malkova, et al., *Kriosfera Zemli*, **21**, No. 3, 69–82 (2017). https://doi.org/10.21782/KZ1560-7496-2017-3(69-82)

44. E. Du, L. Zhao, D. Zou, et al., *Remote Sens.*, **12**, No. 4, 605 (2020). https://doi.org/10.3390/rs12040605

45. L. M. Brekhovskikh, *Waves in Layered Media*, Academic Press, New York (2012).

46. V. L. Mironov, A. Yu. Karavayskiy, Yu. I. Lukin, and I. P. Molostov, *Int. J. Remote Sens.*, **41**, No. 10, 3845–3865 (2020). https://doi.org/10.1080/01431161.2019.1708506

47. https://zenodo.org/record/6683911

48. V. L. Mironov, L. G. Kosolapova, Y. I. Lukin, et al., *Remote Sens. Environ.*, **200**, 240–249 (2017). https://doi.org/10.1016/j.rse.2017.08.007

49. A. A. Shpedt, Yu. N. Trubnikov, and N. Yu. Zharinova, *Euras. Soil Sci.*, **50**, No. 10, 1209–1216 (2017). https://doi.org/10.1134/S106422931710012X

50. M. Abramovitz and I. A. Stegun, eds., *Handbook of Mathematical Functions, with Formulas, Graphs, and Mathematical Tables*, Dover, Mineola (1974).

51. https://www.geotech.ru/ledomer_400_na_bpla/

52. https://www.radsys.lv/en/products-soft/products/prod/26